



# Characterisation of ash particles from co-combustion of bark and sludges from pulp and paper industry

Nils Skoglund<sup>a,\*</sup>, Mikael Thyrel<sup>b</sup>, Jonathan Perrin<sup>c</sup>, Anna Strandberg<sup>a,b</sup>

<sup>a</sup> Umeå University, Department of Applied Physics and Electronics, Thermochemical Energy Conversion Laboratory, SE 901 87 Umeå, Sweden

<sup>b</sup> Swedish University of Agricultural Sciences, Department of Forest Biomaterials and Technology, SE 901 83 Umeå, Sweden

<sup>c</sup> Anatomix Beamline, Synchrotron SOLEIL – L'Orme des Merisiers – Départementale 128, 91190 Saint-Aubin, France

## ARTICLE INFO

### Keywords:

X-ray micro-tomography  
Micro-CT  
Biosludge combustion  
Ash particle  
Synchrotron-based analysis  
Nutrient recycling

## ABSTRACT

Recycling phosphorus from waste streams for fertilization purposes could contribute to a sustainable society. The production in the pulp and paper industry results in several waste streams, among others nutrient-rich sludges in different forms. This study presents a detailed chemical and 3D characterization of ash from co-combustion of bark and two types of sludges from a paper mill; mixed sludge and biosludge. The combustion performance was investigated for these experiments and advanced analysis methods were used to characterise the ashes to correlate chemical and physical properties relevant for nutrient recycling. The elemental composition was determined by energy-dispersive X-ray spectroscopy; dominating crystalline phases by X-ray diffraction; and morphology, porosity, pore size distribution and active surface area of the slag were analysed with synchrotron-based X-ray micro-tomography and image analysis. Slag was formed in all combustion experiments to a large extent with increasing amounts with a higher proportion of sludge. Nutrient amounts indicate that slag particles from co-combustion of both biosludge and mixed sludge can be useful either as a soil improvement directly or for recovery processes. Slag from combustion of 30 wt% biosludge and 70 wt% bark contained the highest amount of phosphorus, 9 wt% on a C and O free basis. Evaluation of tomography data showed that discrete and open pores could be distinguished on a micrometre scale. The porosity of the slag varied between the replicates and fuel mixtures, on average between 17 and 23 vol% for the bark and sludge mixtures. Open pore volume displayed large variations, on average 39–56 vol% of the pores were open pores connected to the surrounding volume. For all samples, 90 % of the pores were small, with an equivalent diameter under 30 µm, but the largest pore volume (80–90 %) consists of pores with an equivalent diameter over 75 µm. In soils, pores with a minimum equivalent diameter over 30 µm generally transmit water and the smaller pores store water. The slag particles have relatively thick walls, with few pore openings to the surroundings, indicating that the slag needs to be pre-treated by milling or crushing before application in the soil.

## 1. Introduction

The pulp and paper industry is a large industry, the pulp and paper production in the world was 420 million tonnes in 2018, of which 90 million tonnes were produced in Europe (CEPI 2019 [1]). For the production, wood as raw material undergoes many mechanical and chemical processes several residual streams are produced as by-products. Further, huge amounts of sludge in different forms are produced in wastewater treatment plants at pulp and paper mills.

Landfilling has previously been a common way to treat the sludge after dewatering, but more stringent regulations promote the recovery

of material and energy [2,3]. Regulations, environmental issues, and economical aspects promote the pulp and paper industry to apply feasible solutions for valorisation of residual streams. During the last decade, the industry sector has reduced landfilling and waste disposal rates [4]. Combustion is a common way to handle the sludge, recover energy and reduce the volume [5].

It has been challenging to find ways to recycle the ashes generated at different energy recovery systems [4]. Biosludge can contain large amounts of macro-and micronutrients, but the concentration varies for various production processes and different mills [6]. Increased knowledge may open up for increased nutrient recovery from residual ashes

\* Corresponding author.

E-mail address: [nils.skoglund@umu.se](mailto:nils.skoglund@umu.se) (N. Skoglund).

<https://doi.org/10.1016/j.fuel.2023.127597>

Received 15 December 2022; Received in revised form 10 January 2023; Accepted 22 January 2023

Available online 25 January 2023

0016-2361/© 2023 The Author(s). Published by Elsevier Ltd. This is an open access article under the CC BY license (<http://creativecommons.org/licenses/by/4.0/>).

where phosphorus is of particular interest. Today, the supply of phosphorus is mainly based on phosphate rocks and minerals, which The European Commission has categorised as critical raw materials because of their economic importance and high supply risk [7]. For a sustainable society, it is crucial to recover phosphorus from bio-resources and residual streams.

Biosludge has a high moisture content, high ash content and low calorific value. Therefore, it is necessary to co-combust sludge with another fuel to ensure the stability of combustion conditions. Bark is a typical residual stream from pre-treatment of wood at pulp and paper mill. Burning sludge in the bark boiler can be done with reduced steam generation and boiler efficiency [6]. Grimm et al. [8] have also shown that bark and chemical sludge mixtures were less prone to slagging during combustion than mono-combustion of bark.

The objective of this study was to investigate possibilities for utilising nutrient-rich ash fractions from the combustion of five different fuel compositions consisting of bark and two types of sludges, which are residuals streams from the bioenergy sector. To clarify the potential of these residual streams, the combustion performance was investigated, and advanced analysis methods were used to characterise the ashes and correlate chemical and physical properties relevant for nutrient recycling of the ashes. The characterisation includes evaluating morphology, porosity, pore size distribution and active surface area of ashes with synchrotron-based X-ray micro-tomography (XRT). Additionally, the samples were evaluated according to elemental composition by energy-dispersive X-ray spectroscopy (SEM-EDS) and crystalline phases by X-ray diffraction (XRD) of the samples.

## 2. Material and method

### 2.1. Materials and pre-treatment

#### 2.1.1. Raw materials

Wastewater treatment sludge was collected from a paper mill in Hallstavik, Sweden. The sludges come from two sources: biological sludge and mixed sludge, which contains a blend of primary sludge (fibre sludge) and biological sludge. The mixed sludge contains about 30–35 % biosludge. The fibre sludge is mainly fibre residues but also some inert material. Ferrous sulphate, approximately 15 kg/ton, is added to the sludges before dewatering. The ash content is more than twice as high in biosludge than mixed sludge (16.9 wt% compared to 7.0 wt% on a dry basis). On a relative basis, the mixed sludge has a much higher Si content compared to the biosludge, while the biosludge has a higher content of Fe. Scots pine bark from a sawmill in the province of Västerbotten, Northern Sweden, was mixed with the biosludge. Bark is a typical residual stream from pre-treatment of wood at pulp and paper mills and its admixing with sludges generated on-site facilitates the thermal treatment of sludges on site. Such thermal treatment of sludge

on the industrial site does not result in gate fees from waste transport for external processing.

#### 2.1.2. Fuel mixtures and pelletising

The sludges were dried at 105 °C and then ground using a Kamas BAC-50 hammer mill fitted with a 5-mm sieve. The bark was ground with a Buhler DFZK-1 equipped with a 4-mm sieve. The fuels and the pellets were analysed using an accredited laboratory. The ash content was analysed according to EN 15403:2011 (ALS, ISO 18122) and the main elements C, H, and N with EN ISO 16948:2015 and EN ISO 21663:2020. Cl and S were analysed according to the standard EN 15408:2011 and other ash-forming elements with ICP-SFMS according to EN ISO 17294–1, 2 (mod) and EPA-method 200.8 (mod), and ICP-AES according to EN ISO 11885 (mod) and EPA-method 200.7 (mod)). The relative content of the main ash forming elements is compiled in Fig. 1, a complete list of all detected ash forming elements can be found in Table S1 in Supplementary material.

Mixtures were designed based on the content of ash-forming elements in the raw materials and practical considerations (Fig. 1) to simultaneously improve combustion properties of sludges but also to facilitate the use of resulting ashes with particular focus on P. With 30 wt % sludge, the elemental contribution from the sludge to the ash forming elements were high, and the content of P was relatively large. A higher share of sludge is difficult to apply in practice due to the high ash content in the biosludge. 10 wt% of sludge was also chosen, then the elemental contribution from the bark is more prominent. In addition to P, one difference that may be important for phosphate formation is that of the alkali metals. The total relative amount is quite similar in the respective fuel mixture, but with more sludge, the amount of K decreases while Na increases. Fe and Ca are also affected, with Fe increasing while Ca decreases with more sludge added. The same ratio was selected for both types of sludges and calculated on a dry basis. The fuels were mixed with a ribbon mixer.

The fuels were pelletised in a pilot-scale pellet press, SPC PP 150 pellet mill (Sweden Power Chippers, Borås) with a stationary Ø8 mm ring die. A total of five pellet assortment were produced: 100 % bark (B100), 10 wt% mixed sludge and 90 wt% bark (MSB90), 30 wt% mixed sludge and 70 wt% bark (MSB70), 10 wt% biosludge and 90 wt% bark (BSB90), and 30 wt% biosludge and 70 wt% bark (BSB70).

### 2.2. Combustion

Each pellets assortment were combusted in a horizontal underfed pellet burner (Ecotec BioLine 50), installed in a boiler (Eryl, Falun, Sweden). The boiler has an integrated water-cooled heat exchanger. The boiler has previously been described elsewhere [8]. The feed rate varied between 8.5 kg/h for bark and 8.8–9.4 kg/h for the mixed bark and biosludge fuels. The combustion test lasted for 4–6 h. The temperature

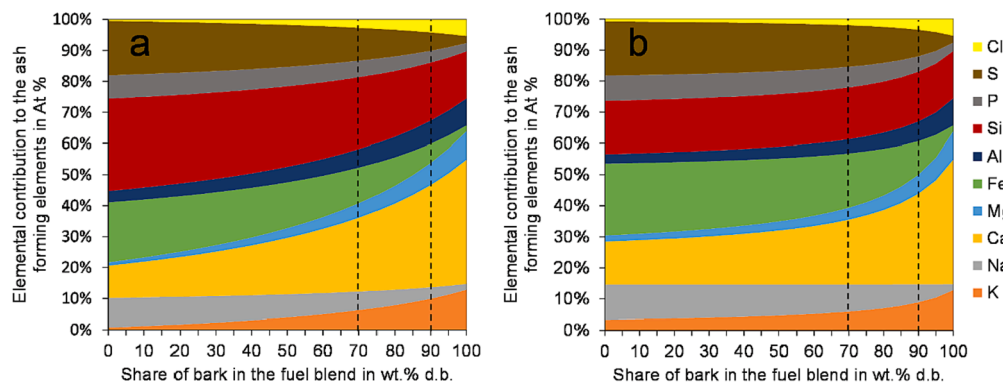


Fig. 1. The elemental contribution of the ash forming elements in at% for the fuel mixtures of a) bark and mixed sludge, and b) bark and biosludge. The share of bark in the fuel blend is indicated on the x-axis. The dashed lines indicate the fuel mixtures used in the present work.

was measured continuously during combustion with two shielded type N thermocouples in and just above the burner grate. A gas analyser (Ecom J2KN-pro Messtechnik GmbH, Germany) continuously measured O<sub>2</sub>, CO<sub>2</sub>, CO, NO, NO<sub>2</sub> and SO<sub>2</sub> in the flue gas, with sampling every second. The combustion procedure started with the feeding of softwood pellets until a steady state was obtained. A small amount of the collected ash and deposits may therefore originate from the softwood pellets; however, the maximum contribution would range between 2.6 % and 0.8 % of the ash residue for the different experiments (calculated values).

After each experiment and cooling, the residual matters were collected, sieved and quantified. The ashes were classified and separated into a) slag particles (previously melted ash) from the burner grate, or particles pushed over the edge down to the bottom of the boiler, >3.15 mm; b) particles in the burner grate at a size of 1.4–3.15 mm; c) non-melted ash in the burner, under the size of 1.4 mm; d) non-melted ash particles >3.15 mm at the bottom of the boiler (bottom ash); e) bottom ash particles at a size of 1.4–3.15 mm; and f) bottom ash under the size of 1.4 mm. Deposit samples were collected from the heat exchanger of the boiler.

### 2.3. Ash characterisation

#### 2.3.1. Scanning electron microscopy analysis (SEM-EDS)

A variable-pressure scanning electron microscope (SEM; Carl Zeiss Evo LS-15) with an energy-dispersive X-ray spectroscopy detector (EDS; Oxford instruments, detector X-Max 80 mm<sup>2</sup>) was used to determine the elemental composition of the ashes. SEM-EDS analysis was performed at low vacuum mode at 50 Pa, with a beam accelerating voltage of 15 kV and probe current of 750 pA. The samples over 1.4 mm were milled prior to analysis to ensure that all parts of the particles were included in elemental analysis rather than only surfaces. A part of the resulting milled and powdery samples was transferred to carbon tape for subsequent analysis. Three replicates from each ash fraction were analysed, and from each replicate, four area analyses were performed (1.5 mm × 1.1 mm) each.

#### 2.3.2. Powder X-ray diffraction (XRD)

For determine crystalline phases in the samples, XRD analysis was performed with a PANalytical Xpert3 Powder XRD in  $\theta$ - $\theta$  mode, with a Cu-K $\alpha$  radiation and a Vântec-1 detector. The samples were continuously rotating during scanning in a range from 10° to 70°. Collected diffractograms were evaluated with the PDF-4 + database in Diffrac.EVA 4.2 for identification of crystalline phases.

XRD analysis was performed on grounded powder from the slag particles from the burner grate and on the bottom ash under the size of 1.4 mm. These are the fractions with the largest amounts of phosphorus, and therefore most suitable for any ash recycling strategy.

#### 2.3.3. X-ray microtomography (XRT) and image analysis

Analysis of morphological parameters and porosity were performed on slag particles at the beamline Anatomix of Synchrotron SOLEIL, France [9]. The scans were conducted with an electron beam current of 100 mA in the storage ring and the polychromatic ('white') X-ray beam used for the measurements had a central photon energy of around 40 keV. The sample was mounted on a rotating stage, and the scans were performed over a range of 180°. For samples not fitting inside the field of view, extended-field tomography was conducted over a range of 360°. The field of view was 6.5 mm, and the pixel size 3.07  $\mu$ m. 1600–5900 projections were collected during each scan with a digital camera (ORCA Flash 4.0 V2), with a lens of 2 × magnification. The exposure time was 10–50 ms. Three particles originating from the slag in the burner grate from each combustion experiment were scanned, and 2–3 scans were added vertically to cover the entire particle.

Reconstruction of collected projections to create 2D images was performed with the reconstruction software PyHST2 [10], which uses the filtered back-projection algorithm for computing the slices of the

reconstructed volume. A double flatfield algorithm was used for decreasing ring artefacts and the Paganin filter for semi-quantitative phase retrieval [11,12].

The data analysis was performed on the reconstructed 3D stack of image files at 8-bit, where each voxel contains a grayscale value between 0 and 255, which corresponds to the X-ray attenuation that is affected by differences in density and atomic number of elements in the scanned object. Areas/voxels with low attenuation, such as pores and air, have a low number on the grayscale, resulting in dark levels on the images, while areas with high attenuation, in this case, the ash contain higher number on the grayscale and bright levels on the images (Fig. 2). The software packages Fiji (Fiji Is Just ImageJ) [13,14] and Avizo 9.3 (Fei VSG Inc., Burlington, MA, USA) were used for image analysis.

With image analysis, the porosity, open pore volume, number of discrete pores, pore size distribution, the thickness of the particle walls and active surface area were computed for all samples. A detailed description of the methods used is given in Strandberg et al. [15]. The images were first processed with binary segmentation, where each voxel in the volume was assigned to either pore/background or ash in the matrix (Fig. 2). This was performed with manual segmentation using visually selected threshold values. The samples contain pores that are completely enclosed in the ash particle (named discrete pores), as well as pores that are connected to the surrounding background (named open pores). The pore volume and pore size (estimated by the equivalent diameter) has been calculated.

The average particle wall thickness was determined with a distance map algorithm (Chamfer Distance Map). The average thickness of the material was then calculated between pores and/or particle surface. The surface area of the ash particle was achieved with a polygonal surface mesh, without smoothing or simplifications. Then the specific surface area was computed by dividing the surface area by the volume of the ash particle. The sphericity was also calculated for the pores. Pores that are not a sphere will have sphericity less than one. Sphericity show how spherical the pores are and can be represented by the following formula:  $\varphi = \pi^{1/3}(6V)^{2/3}/A$ , where V and A are the volume respective surface area of a pore.

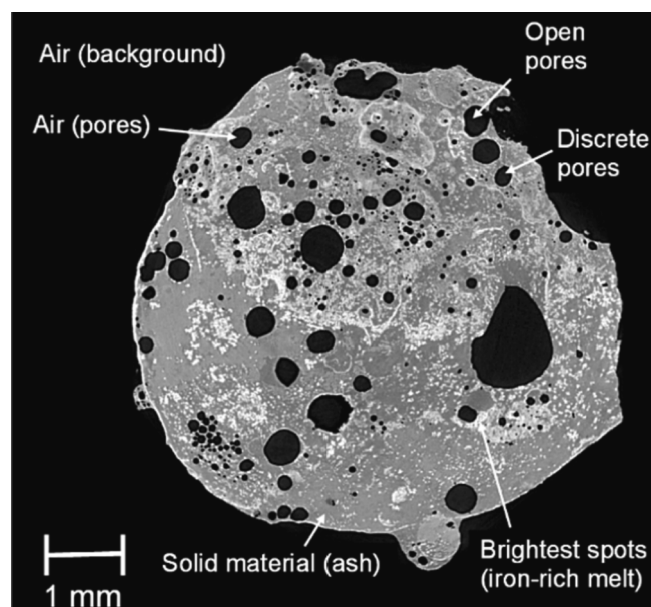


Fig. 2. A XRT cross-section of BSB70 replicate 1, visualising the features used for image analysis.

### 3. Results and discussion

#### 3.1. Combustion performance

The fuel feeding of pellets worked well for all assortments. The average oxygen level during combustion varied between 8.1 and 9.5 vol % (Table 1) and was relatively constant during the respective experiment. The average temperatures measured in and above the burner grate are provided in Table 1 and indicate the temperature regimes during combustion. However, the exact maximum temperature will of course vary in different places in the burner grate and the boiler.

Fig. 3 shows how the flue gas composition varied with the fuel. The CO concentrations were much higher during the combustion of 100 % bark compared to the mixed fuels, and the large error bars indicate a considerable variation during the run. The SO<sub>2</sub> and the NO<sub>2</sub> concentration increased with a higher share of sludge, with the highest levels for biosludge. The concentrations of SO<sub>2</sub> and NO were dependent on the content of N and S in the fuels, with higher levels for biosludge compared to the mixed sludge.

Slag was formed in the burner grate after all experiments. The amount of slag formed varied between the fuels (Table S2, Supplementary material). With 22 wt% of fuel ash that formed slag, bark was less prone to slagging than the sludge mixtures. These results diverge from Grimm et al. [16], who co-combusted bark and chemical sludge using the same combustion system. The difference is assumed to be due to the large amount of Al in the sludge of Grimm et al., which counteracts slag formation. The amount of slag formed in this project increased with a higher share of sludge, with the highest percentage of fuel ash forming slag for the mixture BSB70 (64 wt%) followed by MSB70 (53 wt%). For MSB90 and BSB90, 41 wt% respective 37 wt% of the fuel ash formed slag. With a higher share of sludge, the relative Si content increase, while Ca content decreases (see Fig. 1 and Table S1, Supplementary material), which has previously been shown to increase slag formation [17–19]. Deposits were collected at the heat exchangers, but no cyclone ash could be found in the fly ash collector for any of the runs. The compositional values for the ingoing fuel ash in Table S2 (Supplementary material) is calculated from the fuel used and the ash content (Table S1, Supplementary material). Unburned carbon remained in the ash fractions, except from the slag (see more in chapter 2.3), explaining the higher amount of collected ash compared to ingoing fuel ash.

#### 3.2. Characterisation of ashes

##### 3.2.1. Elemental composition

Fig. 4a shows the average relative composition in the slag. The slag contains significant amounts of Si, most in B100, MSB90 and MSB70. There is also more Si in the mixed sludge compared to the biosludge. The slag contains between 4 and 9 at% of P, with a higher amount for the biosludge than mixed sludge and an increased amount with more sludge in the fuel mixture. As a comparison, a compilation of untreated sewage sludge ash shows an average elemental concentration of 7.6 % [20]. Na is increasing with more sludge in the fuel mixture, almost with the same amount as for P. K, on the other hand, is decreasing with more sludge.

**Table 1**

The oxygen level and temperature in and above burner grate for the respective experiment. The values are given as average during steady-state, with one standard deviation.

	B100	MSB90	MSB70	BSB90	BSB70
O <sub>2</sub> (vol%)	9.5 ± 0.5	8.4 ± 0.6	8.5 ± 0.8	8.1 ± 0.9	9.1 ± 0.9
T in burner grate (°C)	1135 ± 63	1188 ± 72	895 ± 66	890 ± 49	871 ± 66
T above burner grate (°C)	803 ± 32	790 ± 34	885 ± 50	867 ± 37	783 ± 117

Apart from B100 (with more Ca and K, and less Si), the relative composition of the particles in the burner grate at a size of 1.4–3.15 mm (Fig. 4b) is similar to that of larger slag particles. For the non-melted ash in the burner under 1.4 mm (Fig. 4c), relatively more Ca, K and S were found than for larger size fractions. Some remaining carbon was found together with the ash. There was notable amounts of unburned carbon from the fuel left in the bottom ash suggesting that fuel particles from which they originate have not undergone full conversion and therefore has experienced lower temperatures, explaining the relatively high proportion of S in Fig. 4d. A large part of the fuel S is usually released to the gas phase under the prevailing temperatures, where a part of it forms SO<sub>2</sub> emissions, but often it is recaptured by the ash constituents in the flue gas [21,22]. The variance in composition increases from slag particles to bottom ash. It is likely that homogenization of ash forming elements is more efficient in slag particles, where the presence of a melt has facilitated the mobility of various cations in the silicate or phosphate matrices (Fig. 4a-b). The ash particles, that are more powder-like as discrete small particles, may therefore resemble their original composition and will therefore have a higher inherent variance in the results obtained from analysis (Fig. 4d). The bottom ash below the size of 1.4 mm contains less Si than the slag but higher amounts of K. Larger fractions of the bottom ash contained higher proportion of unburned carbon, possibly affecting the SEM-EDS analysis due to relative low levels of the ash forming elements (data not shown).

Fig. 5 show the relative composition of the main ash forming elements from the deposits. Evidently, there was surface rust left on the heat exchangers causing high concentrations of Fe in deposits collected in the first two experiments. Fe is therefore removed and the other elements are normalized. Data with Fe are found in Supplementary material Figure S1. There is more Cl in the bark than in the sludges, and it is also more in MSB90 than the other mixtures (Fig. 1). But this does not explain the significant difference seen in Fig. 5. B100 and MSB90 also stands out with more S compared to the other samples. At the same time, a low level of SO<sub>2</sub> concentration in the flue gas can be seen for these (Fig. 3), which indicates S in the fuel causes preferential formation of alkali sulphates over alkali chlorides [21]. With more S in the fuel (MSB70, BSB90, and BSB70), S probable reacts with alkali, and a significant decrease in Cl in the deposits of the heat exchanger tubes can be seen, which is consistent with previous studies [19,23].

##### 3.2.2. Dominating crystalline phases

Slag particles and burner ash (>3.15 mm) were dominated by silicate compounds, primarily variants of åkermanite (Ca<sub>2</sub>MgSi<sub>2</sub>O<sub>7</sub>) which is a polymerized compound that likely has precipitated from a melt. The concentrations of quartz (SiO<sub>2</sub>) were generally very low – altogether, this indicates that the extensive melt observed occurred as a general reaction throughout the silicate matrix. As sludge were added, some whitlockite and merrillite phases were identified, which are phosphate compounds with a general structure of Ca<sub>10-x-y</sub>(K,Na)<sub>x</sub>(Mg,Fe)<sub>y</sub>(PO<sub>4</sub>)<sub>7</sub>. Some phosphates did therefore not only form with sludge addition but they also reached some degree of crystallinity, separating phosphates from the silicate-dominated slag matrix. With increasing amounts of slag, it was also clear that Fe formed magnetite (Fe<sub>3</sub>O<sub>4</sub>).

The bottom ash displayed higher degrees of unreacted extrinsic material, found as quartz, feldspars and similar soil minerals with high crystallite sizes. Especially crystallite sizes suggest that these extrinsic particles were transported with the fuels and were transported to bottom ash – possibly by entrainment – without having sufficient time to participate fully in the formed slag. It was also noted that the low temperatures for bottom ash resulted in compounds more resembling coarse fly ash. CaCO<sub>3</sub> was abundant, K<sub>2</sub>SO<sub>4</sub> was commonly identified, and even KCl could be identified for some samples. These compounds are generally not stable at the burner temperatures shown in Table 1, indicated that they may not have experienced those high temperatures. There were some indications of mainly whitlockites and hydroxyapatite as phosphates.

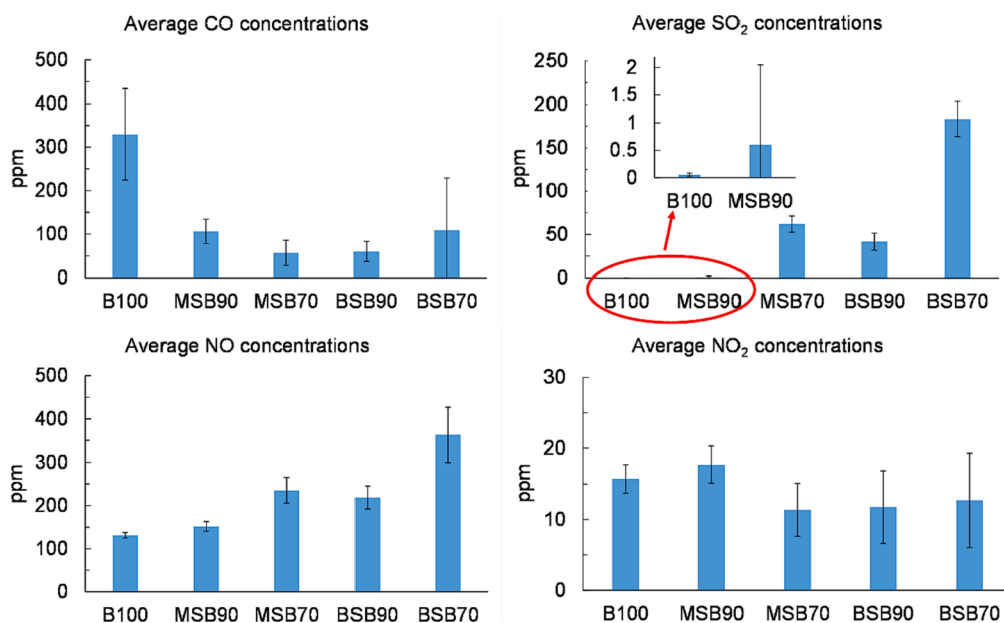


Fig. 3. Average concentrations of CO, SO<sub>2</sub>, NO, and NO<sub>2</sub> in the flue gas as the average during steady-state, provided in ppm<sub>vol</sub> normalised against 10 vol% O<sub>2</sub>. Error bar show one standard deviation.

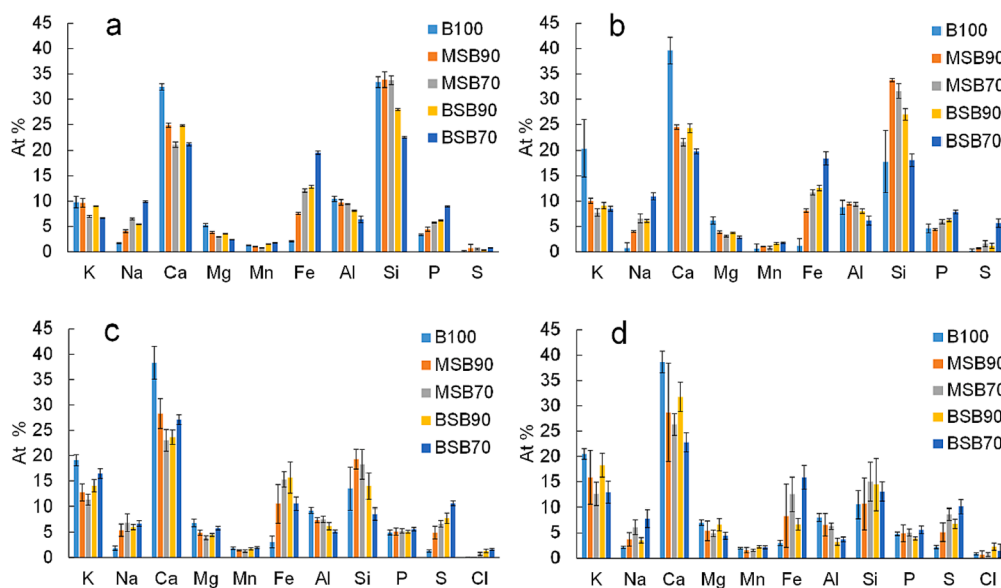


Fig. 4. Relative composition in an average of main ash forming elements on a C and O free basis, in a) the slag found in the burner (>3.15 mm), b) the particles in the burner grate at a size of 1.4–3.15 mm, c) the non-melted ash in the burner under the size of 1.4 mm, and d) the bottom ash under the size of 1.4 mm. Error bars indicate one standard deviation.

### 3.2.3. Morphology, porosity and pore size distribution

Morphology and the pore system of the slag from the combustion experiments were investigated with XRT, at a voxel resolution of 3.07  $\mu\text{m}$ . In Fig. 6, examples of cross-sections of particles from XRT are visualising the heterogeneity of the samples, both in form and content (grayscale). 3D reconstructions of the particles can be seen in Fig. 7.

The calculated average porosity for the particles varied between 12 and 23 vol% (Table 2). The variation between the replicates was large for some samples, which can be seen in the large standard deviation. Table S3, Supplementary material, shows values for each analysed replicate. Slag from pure bark combustion obtained the lowest porosity in average and the lowest average open pore volume. The average detected porosity was highest for MSB70, which also had the highest average open pore volume. Previous research on ash particles from

wheat straw and sewage sludge shows a higher porosity and open pore volume; the average porosity was 62 vol% for wheat straw and 29–31 vol% for the mixtures, and the average open pore volume was between 72 and 99 vol% [15]. Pure wheat straw ash had the highest open pore volume. Wheat straw contains more Si compared to bark. An earlier study has shown that the composition of ash-forming elements in the fuel and the process conditions (e.g. temperature) influence slag formation [18]. The composition (the (K<sub>2</sub>O + CaO)/SiO<sub>2</sub> ratio) and the temperature affect the viscosity of the slag, which affect the behaviour [24], which in turn probably affects pore formation and thus the porosity, open pore volume and surface area of the slag.

The pores are smaller compared to those observed in wheat straw and sewage sludge ashes. Those had an average mean equivalent pore diameter of discrete pores that varied between 24 and 31  $\mu\text{m}$ , compared

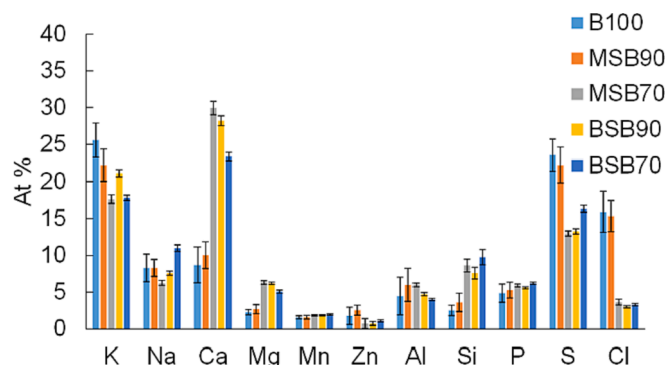


Fig. 5. Relative composition in an average of main ash-forming elements in the deposits collected from the heat exchanger tubes on a Fe, C and O free basis. Error bars indicate one standard deviation.

with 13–19  $\mu\text{m}$  for the samples in this study. However, the resolution was lower for the wheat straw and sewage sludge samples (6.4  $\mu\text{m}$  compared to 3.07  $\mu\text{m}$  in this study), which means that smaller pores could not be observed in the previous work. The number of discrete pores per particle volume is much higher for ash from bark and bio-sludge mixtures (5827–1310 counts/ $\text{mm}^3$ ) compared to wheat straw and sewage sludge ash (580–232 counts/ $\text{mm}^3$ ).

To estimate the durability of the ash particles if applied to the soil, the wall thickness was calculated. The slag particles had relatively thick particle walls. In average the walls were thickest for BSB70, and thinnest for B100 particles. The specific surface area varied in average between 11 and 18  $\text{mm}^2/\text{mm}^3$  for the particles, with no clear trends between the samples. Comparing with ash from wheat straw and wheat straw/sewage sludge mixtures, the specific surface area is larger for the wheat straw ash (31–34  $\text{mm}^2/\text{mm}^3$ ) while the mixtures were more of the same order of magnitude (17–27  $\text{mm}^2/\text{mm}^3$ ) [15]. However, the resolution was lower for those samples. As concluded by Hyväluoma et al. [25], the specific surface area is affected by the resolution and with lower resolution, the visibility of smaller pores and pore wall roughness is limited. This might be a limitation for X-ray tomography. On the other hand, gas adsorption measures at a nanometer-scale resolution, which is of less importance for plant roots, microbes, and water transport [26–28].

Pore openings connected to the environment were examined to assess the ability of roots to penetrate particles and access nutrients. These were measured manually for each particle. As seen in Fig. 7 (middle column with ash particle and pore volume in yellow together), the slag particles have sparse openings at the outer surface to the surroundings, similar for all particles. The openings are also small, most of them with a size of 50–100  $\mu\text{m}$  or less. Some of the particles had larger openings of 300–500  $\mu\text{m}$ . Where the slag has been broken or crushed, there are areas with more and larger openings. Since P is not so mobile [29,30], the particle/root interaction is important for the P uptake. Given the few small openings, the assumption can be made that this type of slag particle needs to be milled or crushed to make it easier for roots to access nutrients.

Pore size distribution has been classified, based on the equivalent diameter, following the definition of the Soil Science Society of America [31] and the criteria proposed by Cameron and Buchan [32], in size ranges of macropores (>75  $\mu\text{m}$ ), mesopores (30–75  $\mu\text{m}$ ), micropores (5–30  $\mu\text{m}$ ), and ultramicropores (0.1–5  $\mu\text{m}$ ). In Fig. 8, counts divided by the total amount of pores are shown in Y1, for all pores (a) respective discrete pores (b), and the volume distribution as the volume share of the total pore volume is shown in Y2 for all pores (a) respective discrete pores (b). According to this classification, the largest number of pores are found as micropores. However, the smallest pores here have an equivalent diameter of 3.8  $\mu\text{m}$  as limitation of the resolution. With a higher resolution that could detect even smaller pores, a higher share of pores might have been classified as ultramicropores, which only hold pores up to 5  $\mu\text{m}$ . Fig. 9 shows the pore size distribution for discrete micropores and ultramicropores for one sample, BSB90\_1, but not divided into classes. This shows that the most significant numbers of pores are found with an equivalent diameter of 3.8  $\mu\text{m}$ . The same applies to the other samples. By far, the largest part of the pore volume consists of macropores. B100 has a higher share of the pore volume in micropores and mesopores compared to the other samples. The pore size distribution can be important for the water holding capacity; generally, in soils, pores with a minimum equivalent diameter over 30  $\mu\text{m}$  transmit water, and the smaller pores store water [32]. The sphericity of the discrete pores decreases with the pore equivalent diameter. As an average, pores with an equivalent diameter of over 20–40  $\mu\text{m}$  is not spherical. The average sphericity for different pore size ranges (equivalent diameter) of the discrete pores is shown in Figure S2 in

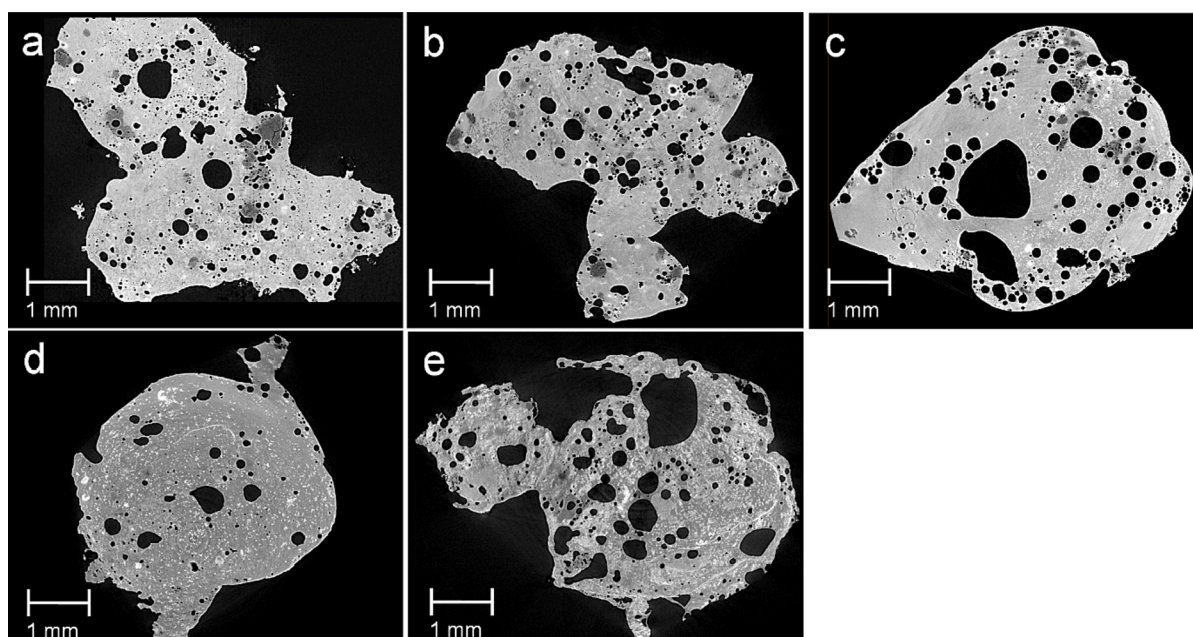
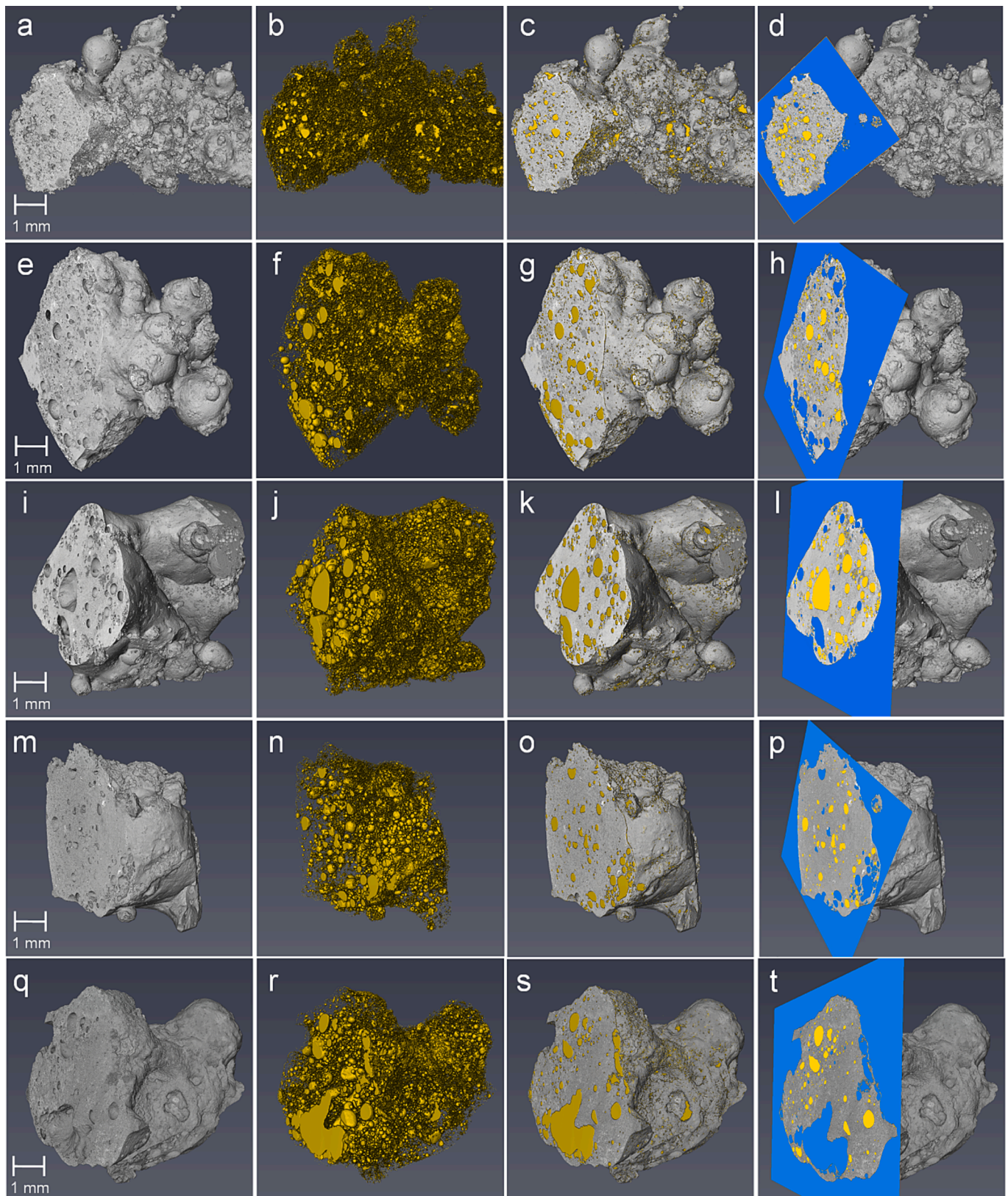


Fig. 6. XRT cross-section of the particle a) B100\_1, b) MSB90\_1, c) MSB70\_1, d) BSB90\_1, and e) BSB70\_1.



**Fig. 7.** Image analysis of the XRT-data with a-d) B100\_1, e-h) MSB90\_1, i-l) MSB70\_1, m-p) BSB90\_1, and q-t) BSB70\_1. The first column from left shows 3D reconstructions of ash particles in grey-scale; the second column show first 3D pore volume (yellow), the third ash particles and pore volume in yellow together, and the right column shows a cross-section of the discrete pores in yellow, background and open-pore volume in blue, together with the ash particle in grey-scale in 3D. (For interpretation of the references to colour in this figure legend, the reader is referred to the web version of this article.)

**Table 2**

Results of image analysis for the particles, showing the average and standard deviation for each fuel mixture.

Sample	Porosity [vol%]	Open pore volume [vol%]	Median/Mean equivalent pore diameter of discrete pores [μm]	No. of discrete pores per particle volume [counts/mm <sup>3</sup> ]	Average wall thickness [μm]	Specific surface area [mm <sup>2</sup> /mm <sup>3</sup> ]
B100	12 ± 2	12 ± 3	10 ± 0/14 ± 1	5827 ± 2840	51 ± 11	14 ± 4
MSB90	18 ± 3	48 ± 13	10 ± 1/14 ± 2	4267 ± 1758	59 ± 19	18 ± 4
MSB70	23 ± 7	56 ± 24	8 ± 3/13 ± 5	1387 ± 317	75 ± 31	17 ± 5
BSB90	18 ± 6	39 ± 14	11 ± 1/17 ± 3	1653 ± 910	82 ± 22	12 ± 4
BSB70	17 ± 3	39 ± 13	12 ± 1/19 ± 0	1310 ± 330	110 ± 40	11 ± 1

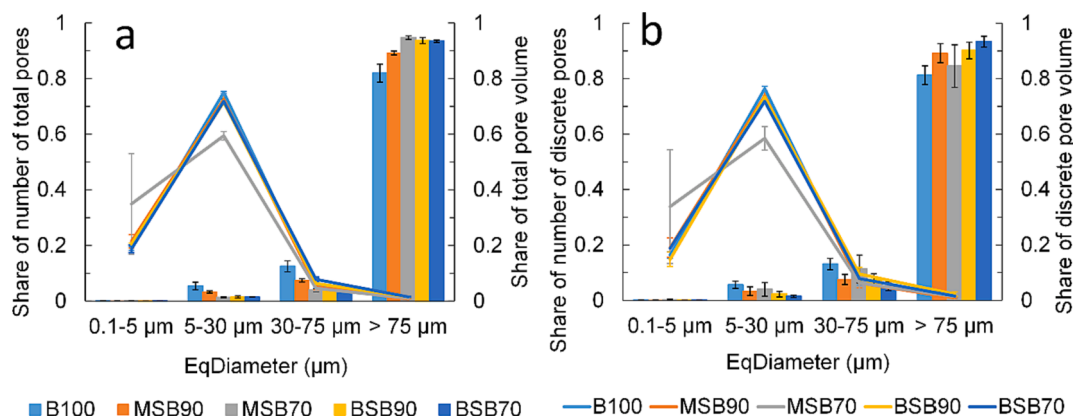


**Fig. 8.** Pore size distribution, showing the share of pores (lines to the left) and share of pore volume (bars to the right) as an average, where a) contains all pores and b) the discrete pores. The pore size is shown as equivalent diameter on the horizontal axis and is divided into size ranges. The error bars represent one standard deviation.

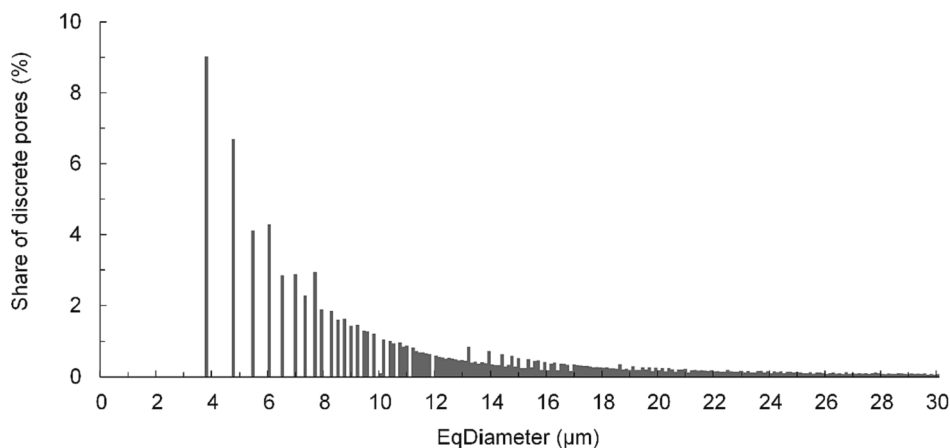


**Fig. 9.** Pore size distribution among micropores and ultramicropores (discrete pores) for BSB90\_1 in percent of the total number of discrete pores.

[Supplementary material \(S1\).](#)

**4. Conclusions**

The amount of nutrients in the slag from the combustion of 30 wt% biosludge and 70 wt% bark indicates that the slag is a candidate material for further investigations on soil improvement, either directly or after further refinement. Slag from the combustion of 30 wt% biosludge and 70 wt% bark contained the highest content of phosphorus, with 9 at% P on a C and O-free basis, followed by 10 wt% biosludge and 90 wt% bark (6.2 at%) and 30 wt% mixed sludge and 70 wt% bark (5.8 at%).

Morphology of slag particles was analysed with synchrotron-based X-ray micro-tomography and image analysis. The porosity and open pore volume of the slag displayed a large variation between replicates and fuel mixtures, with an average porosity between 17 and 23 vol% for the bark and sludge mixtures and in average 39–56 vol% was open pore

volume. The number of discrete pores per particle volume is overall high for ash from bark and biosludge mixtures. The largest relative number of discrete pores were classified as micropores (5–30 μm) or smaller, but the largest volume share of discrete pores consists of macropores (>75 μm). Overall, the slag particles have relatively thick walls, many small discrete pores and with few pore openings to the surroundings, indicating that the slag needs to be ground before application in the soil to improve the root access to the nutrients.

**CRedit authorship contribution statement**

**Nils Skoglund:** Conceptualization, Methodology, Formal analysis, Investigation, Resources, Writing – review & editing, Funding acquisition. **Mikael Thyrel:** Conceptualization, Formal analysis, Resources, Writing – review & editing, Funding acquisition. **Jonathan Perrin:** Formal analysis, Investigation, Resources, Writing – review & editing,

Visualization. **Anna Strandberg:** Conceptualization, Methodology, Formal analysis, Investigation, Resources, Writing – original draft, Writing – review & editing, Visualization, Project administration, Funding acquisition.

### Declaration of Competing Interest

The authors declare that they have no known competing financial interests or personal relationships that could have appeared to influence the work reported in this paper.

### Data availability

Data will be made available on request.

### Acknowledgements

The ÅForsk Foundation, Grant no. 20-618, are acknowledged for financing this work. Bark and chemical analysis of bark were received from the MOBILE FLIP project, which received funding from the European Union's Horizon 2020 research and innovation program under grant agreement number 637020–MOBILE FLIP. Further, the authors gratefully acknowledge the support from Bio4Energy, a strategic research environment appointed by the Swedish government. Nils Skoglund gratefully acknowledges the financial support by Swedish Research Council (Grant no 2017-05331) and FORMAS (Grant no. 2017-01613).

The authors greatly acknowledge the Synchrotron SOLEIL for provision of synchrotron radiation facilities, and we would like to thank Dr Timm Weitkamp for assistance in using beamline ANATOMIX (proposal No. 20201693). ANATOMIX is an Equipment of Excellence (EQUIPEX) funded by the Investments for the Future program of the French National Research Agency (ANR), project NanoimagesX, grant no. ANR-11-EQPX-0031.

The authors also thank the facilities and technical support (Dr Cheng Choo Lee) of the Umeå Core Facility for Electron Microscopy (UCEM) at the Chemical Biological Centre (KBC), Umeå University, National Microscopy Infrastructure, NMI (VR-RFI 2016-00968).

The authors wish to thank Anna Ramberg and Jörg Brücher at Holmen AB for the help and provision of sludges, as well as Gunnar Kahlén and Markus Segerström at Biomass Technology Centre, Department of Forest Biomaterials and Technology, Swedish University of Agricultural Sciences, for grinding, mixing and pelletising the fuels and help with the combustion experiments.

### Appendix A. Supplementary data

Supplementary data to this article can be found online at <https://doi.org/10.1016/j.fuel.2023.127597>.

### References

- [1] Cepi, KEY STATISTICS 2019 European pulp & paper industry, in, <https://www.cepi.org/wp-content/uploads/2020/07/Final-Key-Statistics-2019.pdf>, 2019.
- [2] Directive (EU) 2018/850 of the European Parliament and of the Council of 30 May 2018 amending Directive 1999/31/EC on the landfill of waste, in, Official Journal of the European Union <https://eur-lex.europa.eu/legal-content/EN/TXT/?uri=celex%3A32018L0850>, 2018.
- [3] Council Directive 1999/31/EC of 26 April 1999 on the landfill of waste, in, <http://eur-lex.europa.eu/legal-content/EN/TXT/?uri=CELEX%3A01999L0031-20180704>, 2018.
- [4] LGI, RISE-Processum, Tecnalia, Acciona, UAVR, ZAG, PAPERCHAIN\_D2.3\_Raw materials supply scenario, in, 2018.
- [5] Ouadi M, Fivga A, Jahangiri H, Saghir M, Hornung A. A Review of the Valorization of Paper Industry Wastes by Thermochemical Conversion. *Ind Eng Chem Res* 2019; 58:15914–29.
- [6] Bajpai P, editor. Management of Pulp and Paper Mill Waste. Cham: Springer International Publishing; 2015.
- [7] Communication from the commission to the european parliament, the council, the european economic and social committee and the committee of the regions on the 2017 list of Critical Raw Materials for the EU COM/2017/0490 final, in, <https://eur-lex.europa.eu/legal-content/EN/TXT/?uri=CELEX:52017DC0490>, European Commission 2017.
- [8] Grimm A, Etula J, Salh R, Kalén G, Segerström M, Brücher J, et al. Slagging and fouling characteristics during co-combustion of Scots pine bark with low-temperature dried pulp and paper mill chemical sludge. *Fuel Process Technol* 2019; 193:282–94.
- [9] Weitkamp T, Scheel M, Giorgetta JL, Joyet V, Le Roux V, Cauchon G, et al. The tomography beamline ANATOMIX at Synchrotron SOLEIL. *J Phys Conf Ser* 2017; 849:012037.
- [10] Mirone A, Brun E, Guoullart E, Tafforeau P, Kieffer J. The PyHST2 hybrid distributed code for high speed tomographic reconstruction with iterative reconstruction and a priori knowledge capabilities. *Nucl Instrum Methods Phys Res, Sect B* 2014;324:41–8.
- [11] Paganin D, Mayo SC, Gureyev TE, Miller PR, Wilkins SW. Simultaneous phase and amplitude extraction from a single defocused image of a homogeneous object. *J Microsc* 2002;206:33–40.
- [12] Weitkamp T, Haas D, Wegrzynek D, Rack A. ANKPhase: software for single-distance phase retrieval from inline X-ray phase-contrast radiographs. *J Synchrotron Radiat* 2011;18:617–29.
- [13] Schneider CA, Rasband WS, Eliceiri KW. NIH Image to ImageJ: 25 years of image analysis. *Nat Methods* 2012;9:671.
- [14] Schindelin J, Arganda-Carreras I, Frise E, Kaynig V, Longair M, Pietzsch T, et al. Fiji: an open-source platform for biological-image analysis. *Nat Methods* 2012;9: 676.
- [15] Strandberg A, Skoglund N, Thyrel M. Morphological characterisation of ash particles from co-combustion of sewage sludge and wheat straw with X-ray microtomography. *Waste Manag* 2021;135:30–9.
- [16] Falk J, Skoglund N, Grimm A, Ohman M. Systematic Evaluation of the Fate of Phosphorus in Fluidized Bed Combustion of Biomass and Sewage Sludge. *Energy Fuels* 2020;34:3984–95.
- [17] Näzelius I-L, Fagerström J, Boman C, Boström D, Öhman M. Slagging in Fixed-Bed Combustion of Phosphorus-Poor Biomass: Critical Ash-Forming Processes and Compositions. *Energy Fuels* 2015;29:894–908.
- [18] Boström D, Skoglund N, Grimm A, Boman C, Öhman M, Broström M, et al. Ash Transformation Chemistry during Combustion of Biomass. *Energy Fuels* 2012;26: 85–93.
- [19] Niu Y, Tan H, S.e. Hui. Ash-related issues during biomass combustion: Alkali-induced slagging, silicate melt-induced slagging (ash fusion), agglomeration, corrosion, ash utilization, and related countermeasures. *Prog Energy Combust Sci* 2016;52:1–61.
- [20] Ma P, Rosen C. Land application of sewage sludge incinerator ash for phosphorus recovery: A review. *Chemosphere* 2021;274:129609.
- [21] Hupa M, Karlström O, Vainio E. Biomass combustion technology development–It is all about chemical details. *Proc Combust Inst* 2017;36:113–34.
- [22] Knudsen JN, Jensen PA, Lin W, Dam-Johansen K. Secondary Capture of Chlorine and Sulfur during Thermal Conversion of Biomass. *Energy Fuels* 2005;19:606–17.
- [23] Glarborg P, Marshall P. Mechanism and modeling of the formation of gaseous alkali sulfates. *Combust Flame* 2005;141:22–39.
- [24] Ma C, Skoglund N, Carlborg M, Broström M. Viscosity of molten CaOK<sub>2</sub>SiO<sub>2</sub> woody biomass ash slags in relation to structural characteristics from molecular dynamics simulation. *Chem Eng Sci* 2020;215:115464.
- [25] Hyvaluoma J, Kulju S, Hannula M, Wikberg H, Kalli A, Rasa K. Quantitative characterization of pore structure of several biochars with 3D imaging. *Environ Sci Pollut Res Int* 2018;25:25648–58.
- [26] Brewer CE, Chuang VJ, Masiello CA, Gonnermann H, Gao X, Dugan B, et al. New approaches to measuring biochar density and porosity. *Biomass Bioenergy* 2014; 66:176–85.
- [27] Gray M, Johnson MG, Dragila MI, Kleber M. Water uptake in biochars: The roles of porosity and hydrophobicity. *Biomass Bioenergy* 2014;61:196–205.
- [28] Rasa K, Heikkinen J, Hannula M, Arstila K, Kulju S, Hyvaluoma J. How and why does willow biochar increase a clay soil water retention capacity? *Biomass Bioenergy* 2018;119:346–53.
- [29] Barber SA. Soil nutrient bioavailability: a mechanistic approach. John Wiley & Sons; 1995.
- [30] Lynch J. Root architecture and plant productivity. *Plant Physiol* 1995;109(1):7–13.
- [31] Glossary of soil science terms 2008, in, Soil Science Society of America, Soil Science Glossary Terms Committee 2008.
- [32] Cameron KC, Buchan GD. Porosity: Pore Size Distribution. In: Encyclopedia of soil science. CRC Press; 2017. p. 1782–5.